

# Polarity relevance in flux-rope trajectory deflections triggered by coronal holes<sup>★</sup>

A. Sahade<sup>1,2,3</sup> , M. Cécere<sup>1,3</sup> , A. Costa<sup>1</sup>, and H. Cremades<sup>4</sup> 

<sup>1</sup> Instituto de Astronomía Teórica y Experimental, CONICET-UNC, Córdoba, Argentina  
e-mail: [acosta@unc.edu.ar](mailto:acosta@unc.edu.ar)

<sup>2</sup> Facultad de Matemática, Astronomía, Física y Computación, Universidad Nacional de Córdoba (UNC), Córdoba, Argentina  
e-mail: [asahade@unc.edu.ar](mailto:asahade@unc.edu.ar)

<sup>3</sup> Observatorio Astronómico de Córdoba, UNC, Córdoba, Argentina  
e-mail: [mariana.cecere@unc.edu.ar](mailto:mariana.cecere@unc.edu.ar)

<sup>4</sup> Universidad Tecnológica Nacional–Facultad Regional Mendoza, CONICET, CEDS, Rodríguez 243, Mendoza, Argentina

Received 13 April 2021 / Accepted 23 June 2021

## ABSTRACT

**Context.** Many observations suggest that coronal holes (CHs) are capable of deviating the trajectory of coronal mass ejections (CMEs) away from them. However, for some peculiar events, the eruption has been reported to be initially pulled towards the CH and then away from it.

**Aims.** We study the interaction between flux ropes (FRs) and CHs by means of numerical simulations, with the ultimate goal being to understand how CHs can deviate erupting CMEs/FRs from purely radial trajectories.

**Methods.** We perform 2.5D magnetohydrodynamical numerical simulations of FRs and CHs interacting under different relative polarity configurations. In addition, we reconstruct the 3D trajectory and magnetic environment of a particular event seen by the STEREO spacecraft on 30 April 2012, whose trajectory initially departed from the radial direction toward the CH but later moved away from it.

**Results.** The numerical simulations indicate that at low coronal heights, depending on the relative magnetic field polarity between FR and CH, the initial deflection is attractive, that is, the FR moves towards the CH (case of anti-aligned polarities) or repulsive, where the FR moves away from the CH (case of aligned polarities). This is likely due to the formation of vanishing magnetic field regions or null points located between the FR and CH (case of anti-aligned polarities) or at the other side of the FR (case of aligned polarities). The analysed observational event shows a double-deflection compatible with an anti-aligned configuration of magnetic polarities, which is supported by SDO observations. We successfully reproduce the double deflection of the observed event by means of a numerical simulation.

**Key words.** magnetohydrodynamics (MHD) – Sun: coronal mass ejections (CMEs) – Sun: magnetic fields – methods: numerical – methods: observational

## 1. Introduction

Large amounts of mass and magnetic field detachments are involved in the release of coronal mass ejections (CMEs). Many CMEs show clear indications of an embedded magnetic flux-rope (FR; i.e. magnetic field lines twisted around an axial field) structure. The FR magnetic system, which is usually associated with filaments, frequently deflects from its outward radial direction. This may be caused by multiple factors. For example, intrinsic CME and filament properties may affect the final amount of deflection (e.g. [Filippov et al. 2001](#); [Martin 2003](#); [Panasenco & Martin 2008](#); [Bemporad 2009](#); [Panasenco et al. 2011](#); [Pevtsov et al. 2012](#); [Liewer et al. 2013](#); [Möstl et al. 2015](#); [Wang et al. 2015](#); [Kay et al. 2015, 2017](#)). The magnetic field environment also contributes to the deflection through the interaction of the CME/FR with surrounding structures, such as for example coronal holes (CH, e.g. [Cremades et al. 2006](#); [Xie 2009](#); [Gopalswamy et al. 2009](#); [Kilpua et al. 2009](#); [Panasenco et al. 2013](#)), active regions (e.g. [Kay et al. 2015](#); [Möstl et al. 2015](#)), pseudostreamers (e.g. [Lynch & Edmondson](#)

[2013](#)), streamer belts (e.g. [Zuccarello et al. 2012](#); [Kay et al. 2013](#); [Yang et al. 2018](#)), and heliospheric current sheets (e.g. [Liewer et al. 2015](#)).

Previous reports have suggested that CME trajectories depend on the local and global gradients of the magnetic pressure ([Panasenco et al. 2013](#); [Liewer et al. 2015](#); [Sieyra et al. 2020](#)). The analysed CMEs were found to propagate in the direction of least resistance, away from CHs. This behaviour was also numerically studied by [Sahade et al. \(2020, hereafter S20\)](#), who found that the FR deflection away from the CH was firstly due to the minimum magnetic energy location and secondly to the channelling imposed by magnetic field lines.

Studies based on the evolution of CMEs in the high corona agree on the hypothesis that CHs and open magnetic fluxes, acting as strong ‘magnetic walls’, repel neighbouring CMEs by deflecting their trajectories ([Cremades et al. 2006](#); [Gopalswamy et al. 2009](#); [Gui et al. 2011](#); [Yang et al. 2018](#); [Cécere et al. 2020](#)). However, there are a few peculiar examples for which CME paths behave differently. [Jiang et al. \(2007\)](#) investigated a CME that first evolved toward a CH and later moved away from it. Moreover, [Sieyra et al. \(2020, see their Fig. 14\)](#) found that the trajectories of some of the analysed prominence-CMEs were not always deflected away from CHs.

<sup>★</sup> Animations associated to Figs. 4 and 11 are available at <https://www.aanda.org>

Particularly at low coronal heights, the eruption occasionally approached the CH, even when the trajectory was not directed towards the region of minimum magnetic energy. Yang et al. (2018) studied the interaction of a small filament with non-CH open field lines. The filament polarity was anti-aligned with respect to the polarity of the open magnetic field lines, meaning that the positive polarity footpoint of the filament was adjacent to the negative polarity of the open magnetic fluxes. These latter authors also found that the erupted filament material first approached the open field lines and was then strongly deflected away from them.

To improve our understanding of the interaction between CMEs and CHs, we performed 2.5D MHD numerical simulations of a FR in the low corona. We analysed the resulting trajectory deflection and we studied the initial forces acting on the FR (Sect. 2). We consider both aligned and anti-aligned polarities of the CH open field lines with respect to the nearest FR footpoint polarity. In Sect. 3 we present our study of an eruptive event that interacted with a CH and was observed on 30 April 2012 by the Solar-Terrestrial Relations Observatory (STEREO, Kaiser et al. 2008) twin spacecraft. The CME initially approached the CH and then propagated away from it, in a similar manner to the peculiar observed eruptive events mentioned above. Conclusions and some open questions are presented in Sect. 4.

## 2. Numerical simulation

We performed numerical simulations to study the interaction between a FR and a CH without other interfering magnetic structures. We used a simple 2.5D model that provides meaningful information about magnetic fields and FR dynamics. The interaction is solved through the ideal MHD equations in the presence of a gravitational field. The equations in CGS units in the Cartesian conservative form are written as:

$$\frac{\partial \rho}{\partial t} + \nabla \cdot (\rho \mathbf{v}) = 0, \quad (1)$$

$$\frac{\partial (\rho \mathbf{v})}{\partial t} + \nabla \cdot \left( \rho \mathbf{v} \mathbf{v} - \frac{1}{4\pi} \mathbf{B} \mathbf{B} \right) + \nabla p + \nabla \left( \frac{B^2}{8\pi} \right) = \rho \mathbf{g}, \quad (2)$$

$$\frac{\partial E}{\partial t} + \nabla \cdot \left[ \left( E + p + \frac{B^2}{8\pi} \right) \mathbf{v} - \frac{1}{4\pi} (\mathbf{v} \cdot \mathbf{B}) \mathbf{B} \right] = \rho \mathbf{g} \cdot \mathbf{v}, \quad (3)$$

$$\frac{\partial \mathbf{B}}{\partial t} + \nabla \cdot (\mathbf{v} \mathbf{B} - \mathbf{B} \mathbf{v}) = \mathbf{0}, \quad (4)$$

where  $\rho$  represents the plasma density,  $p$  the thermal pressure,  $\mathbf{v}$  the velocity,  $\mathbf{B}$  the magnetic field, and  $\mathbf{g}$  the gravity acceleration.  $E$  is the total energy (per unit volume), given by

$$E = \rho \epsilon + \frac{1}{2} \rho v^2 + \frac{B^2}{8\pi},$$

where  $\epsilon$  is the internal energy and

$$\mathbf{j} = \frac{c}{4\pi} \nabla \times \mathbf{B}$$

is the current density, with  $c$  being the speed of light.

In addition to the MHD equations, the divergence-free condition of the magnetic field must be fulfilled, that is,

$$\nabla \cdot \mathbf{B} = 0. \quad (5)$$

For completeness, we assume a perfect gas for which  $p = 2\rho k_B T / m_i = (\gamma - 1)\rho \epsilon$ , where  $k_B$  is the Boltzmann constant,  $T$

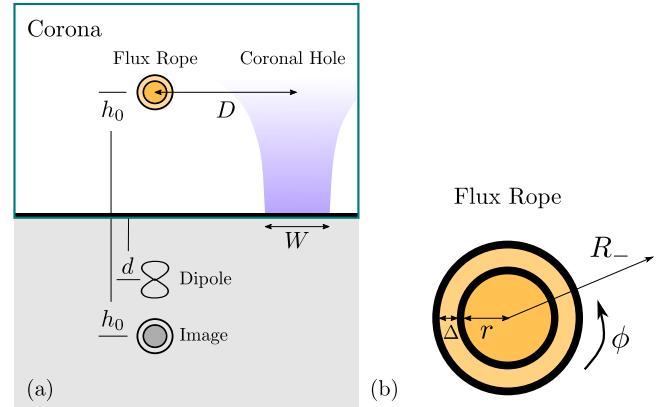


**Fig. 1.** (a) FR and CH scheme not to scale. The turquoise frame indicates the simulated region.  $h_0$  is the FR (orange circle) height and  $D$  is the FR distance to the CH (purple-shaded area) whose width is parametrised by  $W$ . The line dipole and the image current are located at depth  $d$  and  $h_0$ , respectively. (b) Current wire layers:  $r$  is the radius,  $\Delta$  is the thickness of the transition layer,  $R_-$  is the radial coordinate from the FR centre, and  $\phi$  the poloidal coordinate.

the plasma temperature,  $m_i$  the proton mass (assuming that the medium is a fully ionised hydrogen plasma), and  $\gamma = 5/3$  the specific heat relation.

Simulations were performed using the FLASH Code (Fryxell et al. 2000) in its fourth version, operated with the USM (unsplit staggered mesh) solver, which uses a second-order directionally unsplit scheme with a MUSCL-type reconstruction. Outflow conditions (zero-gradient) are used at lateral and upper boundaries, and a line-tied condition is used at the lower boundary. To preserve the initial force-free configuration outside the FR, a linear extrapolation of the magnetic field is established (Zurbriggen, priv. comm.). We can neglect the magnetic resistivity and use the ideal MHD equations. This results in a significant reduction of the computational cost, because the numerical diffusion present in the simulations provides the necessary dissipation (Krause et al. 2018). The highest resolution corresponds to  $\sim [0.1 \times 0.1]$  Mm<sup>2</sup> cells in a  $[-700, 700]$  Mm  $\times$   $[0, 700]$  Mm physical domain, where pressure and temperature gradients satisfy the refinement criterion.

### 2.1. Magnetic model

We depart from an out-of-equilibrium magnetic FR whose general configuration is schematised in Fig. 1. The magnetic field of the FR is produced by a current wire, an image current wire, and a line dipole. The image current is located below the photosphere and has an opposite direction, and so generates a repulsive force. The line dipole located below the photosphere provides an attractive force to the CME wire and emulates the photospheric field. The equations are piecewise-defined in three zones:

Z1 Inside a current wire,  $0 \leq R < r - \frac{\Delta}{2}$ ,

Z2 throughout the transition layer,  $r - \frac{\Delta}{2} \leq R < r + \frac{\Delta}{2}$ ,

Z3 outside a current wire,  $r + \frac{\Delta}{2} \leq R$ ,

where  $r$  is the current wire radius,  $\Delta$  is the thickness of the transition layer between the current wire and the exterior, and  $R$  is the radial coordinate from the centre of the current wire (Fig. 1b).

The magnetic field component  $B_\phi$  generated by a current wire with current distribution  $j_z$  is given by:

$$B_\phi(R) = \begin{cases} \frac{2\pi}{c} j_0 R & \text{at Z1} \\ \frac{2\pi j_0}{cR} \left\{ \frac{1}{2} \left( r - \frac{\Delta}{2} \right)^2 - \left( \frac{\Delta}{2} \right)^2 \right. \\ \quad \left. + \frac{R^2}{2} + \frac{\Delta R}{\pi} \sin \left[ \frac{\pi}{\Delta} \left( R - r + \frac{\Delta}{2} \right) \right] \right. \\ \quad \left. + \left( \frac{\Delta}{\pi} \right)^2 \cos \left[ \frac{\pi}{\Delta} \left( R - r + \frac{\Delta}{2} \right) \right] \right\} & \text{at Z2} \\ \frac{2\pi j_0}{cR} \left[ r^2 + \left( \frac{\Delta}{2} \right)^2 - 2 \left( \frac{\Delta}{\pi} \right)^2 \right] & \text{at Z3,} \end{cases} \quad (6)$$

$$j_z(R) = \begin{cases} j_0 & \text{at Z1} \\ \frac{j_0}{2} \left\{ \cos \left[ \frac{\pi}{\Delta} \left( R - r + \frac{\Delta}{2} \right) \right] + 1 \right\} & \text{at Z2} \\ 0 & \text{at Z3,} \end{cases} \quad (7)$$

where  $j_0$  is a current density.

In order to obtain a helical magnetic field in the FR, we include a magnetic field in the  $z$ -axis of strength  $B_z$ . In this way, as we showed in S20, we avoid excessive gas pressure values needed to balance the magnetic pressure inside the FR in the initial equilibrium state. The component  $B_z$  of the magnetic field and the current distribution  $j_\phi$ , are described by:

$$B_z(R) = \frac{\sqrt{8}\pi j_1}{c} \sqrt{\left( r - \frac{\Delta}{2} \right)^2 - R^2}, \quad (8)$$

$$j_\phi(R) = j_1 R \left[ \sqrt{\left( r - \frac{\Delta}{2} \right)^2 - R^2} \right]^{-1}, \quad (9)$$

where  $j_1$  is a current density. These expressions are valid inside the FR (Z1) and are null in the rest of the domain.

For the initial magnetic field of the CH, we use the same expressions as in S20. The total initial magnetic field is the sum of the magnetic field of the FR and the magnetic field of the CH, which in Cartesian components is given by:

$$\begin{aligned} B_x &= B_0 \sin \left( \frac{x-D}{W} \right) \exp[-y/W] - B_\phi(R_-) \frac{(y-h_0)}{R_-} \\ &\quad + B_\phi(R_+) \frac{(y+h_0)}{R_+} - MdB_\phi \left( r + \frac{\Delta}{2} \right) \left( r + \frac{\Delta}{2} \right) \frac{x^2 - (y+d)^2}{R_d^2}, \\ B_y &= B_0 \cos \left( \frac{x-D}{W} \right) \exp[-y/W] + B_\phi(R_-) \frac{x}{R_-} \\ &\quad - B_\phi(R_+) \frac{x}{R_+} - MdB_\phi \left( r + \frac{\Delta}{2} \right) \left( r + \frac{\Delta}{2} \right) \frac{2x(y+d)}{R_d^2}, \\ B_z &= B_z(R_-), \end{aligned} \quad (10)$$

where the parameter  $B_0$  is the radial magnetic field strength of the CH at the distance  $D$  on the  $x$ -axis. The parameter  $W$  is related to the width of the CH (see following subsection) and modifies the decay of the magnetic field strength in the  $y$ -direction.  $h_0$  is the initial vertical position of the FR and  $M$  is the intensity of the line dipole at depth  $d$ . The distances  $R$  are:

$$R_\pm = \sqrt{x^2 + (y \pm h_0)^2},$$

$$R_d = \sqrt{x^2 + (y+d)^2},$$

where  $R_-$ ,  $R_+$ , and  $R_d$  originate in the FR centre, image current wire, and line dipole, respectively (see Fig. 1 of S20 for more details).

## 2.2. Thermodynamic variables

We simulate the solar atmosphere by adopting a multi-layer structure (Mei et al. 2012). The chromosphere lies between  $y = 0$  and  $y = h_{\text{ch}}$  with constant temperature  $T_{\text{ch}}$ . The transition

region, located between  $y = h_{\text{ch}}$  and the base of the corona ( $y = h_c$ ), is represented by a linearly increasing temperature up to  $T_c$ , which is the constant temperature assumed for the corona. The initial temperature distribution is given by

$$T(y) = \begin{cases} T_{\text{ch}} & \text{if } 0 \leq y < h_{\text{ch}} \\ (T_c - T_{\text{ch}}) \left[ \frac{y-h_{\text{ch}}}{h_c-h_{\text{ch}}} \right] + T_{\text{ch}} & \text{if } h_{\text{ch}} \leq y < h_c \\ T_c & \text{if } h_c \leq y. \end{cases} \quad (11)$$

We set a temperature of  $T_{\text{ch}} = 10\,000$  K for the chromosphere and  $T_c = 10^6$  K for the corona. The height of the chromosphere is  $h_{\text{ch}} = 10$  Mm, while the base of the corona is at  $h_c = 15$  Mm.

The temperature inside the FR ( $T_{\text{FR}}$ ) varies according to the following temperature distribution:

$$T(R_-) = \begin{cases} T_{\text{FR}} & \text{at Z1} \\ (T_c - T_{\text{FR}}) \left[ \frac{R_-(r+\Delta/2)}{\Delta} \right] + T_{\text{FR}} & \text{at Z2} \\ T_c & \text{at Z3.} \end{cases} \quad (12)$$

In a previous study (S20), we considered the current-free atmosphere in hydrostatic equilibrium. Hence, the pressure  $p(y)$  was only a function of  $y$  considering a system with a  $y$ -axis aligned to the gravity acceleration (i.e.  $\mathbf{g} = \frac{-GM_\odot}{(y+R_\odot)^2} \mathbf{e}_y$ , where  $G$  is the gravitational constant,  $M_\odot$  is the Sun mass,  $R_\odot$  is the solar radius, and  $y = 0$  corresponds to the solar surface). In the present study, we add a dimensionless factor  $\chi$  to the pressure distribution in order to set a subdense CH (based on the density distributions proposed by Pascoe et al. 2014):

$$\chi(x, y) = \begin{cases} \beta(x, y) + 1 & \text{if } y < W/2 \\ \left( 2 - 2\frac{y}{W} \right) \beta(x, y) + 1 & \text{if } W/2 \leq y < W \\ 1 & \text{if } W \leq y, \end{cases} \quad (13)$$

where

$$\beta(x, y) = \left( \frac{n_{\text{CH}}}{n_c} - 1 \right) \text{sech}^2 \left( \frac{x-D}{W \arcsin(0.25 \exp[y/W])} \right)^2.$$

The number density at height  $y = h_c$  in the corona is  $n_c$ , while inside the CH the number density decays to  $n_{\text{CH}}$ . According to the resulting subdense zone, the effective width of the CH is set to  $w \sim W/2$ . The pressure is then  $P(x, y) = \chi(x, y)p(y)$ , where  $p(y)$  is the hydrostatic component:

$$p(y) = \begin{cases} p_{\text{ch}} \exp \left[ \frac{\alpha}{T_{\text{ch}}} \left( \frac{1}{h_{\text{ch}}+R_\odot} - \frac{1}{y+R_\odot} \right) \right] & \text{if } 0 \leq y < h_{\text{ch}} \\ p_{\text{ch}} \exp \left[ - \int_{h_{\text{ch}}}^y \frac{\alpha}{T(y')} (R_\odot + y')^{-2} dy' \right] & \text{if } h_{\text{ch}} \leq y < h_c \\ \frac{k_B}{N_A m_i} T_c n_c \exp \left[ - \frac{\alpha}{T_c} \left( \frac{1}{h_c+R_\odot} - \frac{1}{y+R_\odot} \right) \right] & \text{if } h_c \leq y, \end{cases} \quad (14)$$

where

$$p_{\text{ch}}(y) = \frac{k_B}{N_A m_i} T_c n_c \exp \left[ \int_{h_{\text{ch}}}^{h_c} \frac{\alpha}{T(y')} (R_\odot + y')^{-2} dy' \right],$$

$\alpha = \frac{m_i G M_\odot}{2k_B}$ , and  $N_A$  is the Avogadro number. The internal pressure of the FR is obtained by proposing a solution close to the equilibrium:

$$\begin{aligned} p_{\text{FR}}(x, y) &= P(x, y) + \frac{1}{c} \int_R^{r+\frac{\Delta}{2}} B_\phi(R') j_z(R') dR' \\ &\quad - \frac{1}{c} \int_R^{r+\frac{\Delta}{2}} B_z(R') j_\phi(R') dR'. \end{aligned} \quad (15)$$

The associated densities are obtained from the equation of state:

$$\rho = \frac{m_i P(x, y)}{2k_B T(y)}. \quad (16)$$

**Table 1.** CH parameters.

| Case | $B_0$<br>(G) | $D$<br>(Mm) | $W$<br>(Mm) |
|------|--------------|-------------|-------------|
| 1    | 0.4          | 150         | 400         |
| 2    | -0.4         | 150         | 400         |
| 3    | 0.8          | 150         | 400         |
| 4    | -0.8         | 150         | 400         |
| 5    | 1.2          | 150         | 400         |
| 6    | -1.2         | 150         | 400         |
| 7    | 1.6          | 150         | 400         |
| 8    | -1.6         | 150         | 400         |
| 9    | 0.8          | 250         | 400         |
| 10   | -0.8         | 250         | 400         |
| 11   | 0.8          | 350         | 400         |
| 12   | -0.8         | 350         | 400         |
| 13   | 0.8          | 150         | 300         |
| 14   | -0.8         | 150         | 300         |
| 15   | 0.8          | 150         | 500         |
| 16   | -0.8         | 150         | 500         |
| 17   | 0.8          | 150         | 600         |
| 18   | -0.8         | 150         | 600         |

**Notes.** Parameter  $B_0$  is the CH magnetic field strength,  $D$  its distance to the FR, and  $W$  is related to its width.

### 2.3. Setup

To perform a 2.5D simulation we assume that the FR and the CH have a symmetry in the  $z$ -direction. A FR of characteristic length  $L_0 \sim 500$  Mm (Berger 2014) is large enough such that the symmetry assumption is appropriate. Given this characteristic length  $L_0$ , the CHs result in areas ( $A \sim wL_0$ ) of between  $7.5 \times 10^4$  Mm<sup>2</sup> and  $1.5 \times 10^5$  Mm<sup>2</sup> (Hofmeister et al. 2017; Heinemann et al. 2019).

We select the same model parameters as in S20 (see their Sect. 2.5 for more details). We vary the CH parameters as in Table 1 to obtain a set of 18 simulations, which are run with two different FRs to obtain more general results. The initial parameters describing FR1 and FR2 simulations are listed in Table 2.

Cases in Table 1 with positive (negative) magnetic strength  $B_0$  are aligned (anti-aligned), meaning that the FR footpoint which is nearest to the CH has positive (positive) polarity, as shown in the left (right) top panel of Fig. 2. We note that the left panels of this figure are equivalent configurations (aligned), as are those on the right (anti-aligned). It is the relative polarity alignment that provides the different scenarios. The cases in the two upper panels represent the two possible relative FR–CH polarities.

### 2.4. Results

As mentioned in S20, a minimum magnetic energy region (hereafter null point) arises at the position where the magnetic field of the CH and FR counteract (green circles of Fig. 2). The FR–CH aligned polarity cases with positive  $B_0$  have the null point to the left of the FR (negative  $x$ -positions; see top left panel of Fig. 2); while the FR–CH anti-aligned polarity cases with negative  $B_0$  have the null point to the right of the FR (positive  $x$ -positions; see top right panel of Fig. 2). We note that the anti-aligned cases have the null point between the FR and the CH. For both configurations, we calculate the forces acting on the FR centre at  $t = 0$  s. We find that the magnetic force is the main contribution

**Table 2.** Initial state parameters.

| Parameter                           | Value           |                    |
|-------------------------------------|-----------------|--------------------|
|                                     | FR1             | FR2                |
| $j_0$ (stA cm <sup>-2</sup> )       | 435             | 295 <sup>(a)</sup> |
| $j_1$ (stA cm <sup>-2</sup> )       | 455             | 300                |
| $T_{\text{FR}}$ (MK)                | 1               | 4                  |
| $n_c$ (cm <sup>-3</sup> )           | $3 \times 10^8$ | $4.5 \times 10^8$  |
| $n_{\text{CH}}$ (cm <sup>-3</sup> ) | $2 \times 10^8$ |                    |
| $h_0$ (Mm)                          | 30              |                    |
| $r$ (Mm)                            | 2.5             |                    |
| $\Delta$ (Mm)                       | 0.25            |                    |
| $d$ (Mm)                            | 3.125           |                    |
| $M$                                 | 1               |                    |

**Notes.** Parameters  $j_0$  and  $j_1$  are the current densities inside the FR in the  $z$ -direction and  $\phi$ -direction, respectively,  $T_{\text{FR}}$  is the internal FR temperature,  $n_c$  is the numerical density at the base of the corona,  $n_{\text{CH}}$  is the numerical density for the CH,  $h_0$  is the vertical position (height) of the FR,  $r$  is its radius, and  $\Delta$  is the thickness of the transition layer between the FR interior and the corona. Parameters  $d$  and  $M$  are the depth of the line dipole below the boundary surface and its relative intensity, respectively. <sup>(a)</sup>The value  $j_0$  for FR2 was corrected following a typo in S20.

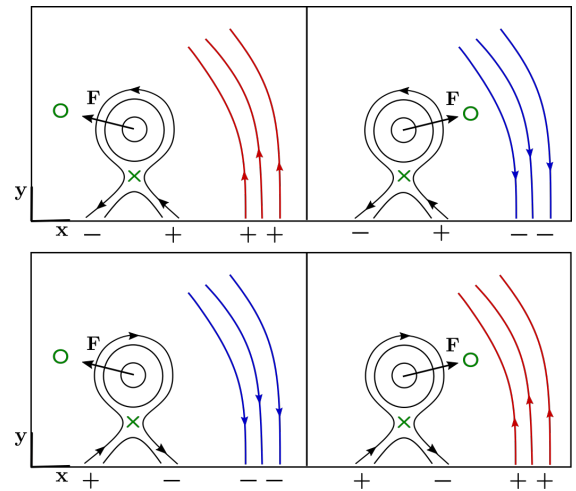


**Fig. 2.** Relative polarity scheme. *Left panels:* cases with aligned FR and CH polarities, for which a null point (green circle) forms on the opposite of the CH. *Right panels:* anti-aligned configuration, for which the minimum forms between the FR and the CH. The forces  $F$  acting on the FR centre are directed towards the null point. The green  $\times$  symbols indicate the site of reconnection.

to the total force. The magnetic force of the simulated cases always points towards the magnetic null point, initially deflecting the FR towards this position. In the aligned cases, the magnetic force points towards a direction away from the CH. The opposite occurs for the anti-aligned cases.

Figure 3 displays the aligned case 7 (negative  $x$  values) and the anti-aligned case 8 (positive  $x$  values) for FR2. In the figure we show the initial null-point locations (blue circles), the initial magnetic forces on the FR centre (cyan arrows), and the resulting trajectories. The last point plotted corresponds to the time when the trajectory becomes parallel to the magnetic field: 700 s for case 7 and 1200 s for case 8. The trajectory of case 7 (dashed-line) deflects only once to the left, while that of case 8 (dotted-line) is first deflected to the right and later to the left, that is, the FR suffers a double deflection. The general dynamics

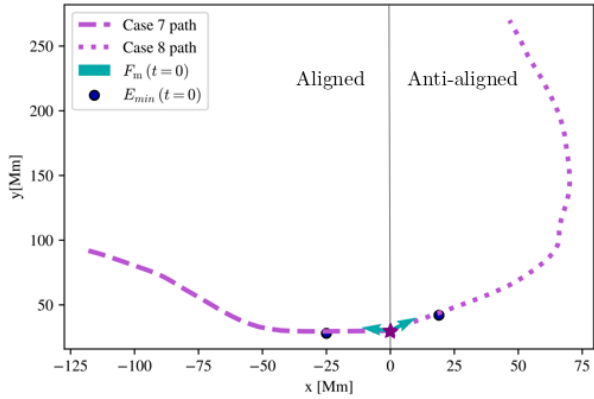


**Fig. 3.** Paths of the FR centre as a function of time (dashed line: aligned case, dotted line: anti-aligned case). The purple star indicates the initial position of the FR centre, the blue circles the initial position of the magnetic null point ( $E_{\min}$ ), and the blue arrows the magnetic force direction on the FR ( $F_m$ ) at  $t = 0$  s.

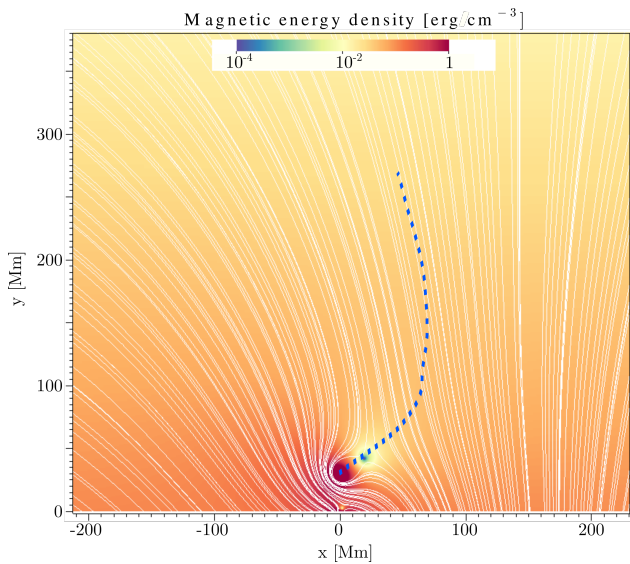


**Fig. 4.** Initial magnetic energy distribution and magnetic field lines for case 8. The dotted line represents the path of the FR centre as a function of time until  $t = 1200$  s. The animated evolution of this figure is available [online](#).

of the aligned cases are represented by case 7, while the anti-aligned cases are represented by case 8. It follows that the single or double deflection depends solely on the relative alignment of the FR and CH polarities.

To explain the double-deflection mechanism seen in anti-aligned cases, we analysed the evolution of the magnetic energy density, also considering the magnetic field lines. Figure 4 (see animation available [online](#)) displays the initial magnetic energy distribution and the magnetic field lines for case 8. The maximum energy (red in the colour scale) is located at the FR centre and the minimum (blue in the colour scale) is located between the FR centre and the CH. The background energy decays with height along the  $y$ -axis. Initially, the FR travels towards the null point and collides with it. The null point then stretches, leading to a low magnetic energy region that surrounds the FR front. A turbulent zone is excited in this region of low magnetic energy, whose plasma parameter  $\beta \approx 1$ , entangling the magnetic field lines. The FR continues moving in the original direction, driving a coronal shock wave that compresses and bends the field

lines. This results in a magnetic force that eventually slows down the lateral motion of the FR, redirecting its trajectory to finally become parallel to the field lines. In summary, in the low corona and for an anti-aligned case, the magnetic force appears as the main driver of the FR trajectory evolution: it is firstly attracted toward the null point, then it surpasses the null-point position due to inertia, until the magnetic force exerted by the compressed and bent CH magnetic field lines pushes the FR away. The final FR path is that of least resistance, that is, it travels guided by the magnetic field lines towards a region of less magnetic energy. Thus, at later stages of evolution, all FRs move away from the CH, independently of the polarity configuration, guided by the magnetic field.

Figure 5a shows the null-point locations for all cases in Table 1 for the FR1 and FR2 (Table 2). For reference, we show the location of the FR centre (purple star). We note that for a given parameter  $W$ , at a given distance  $D$ , there is a linear correlation between the location of the null point and the magnetic field strength  $B_0$ . The larger the magnetic field strength, the closer the null point is to the FR centre. In Fig. 5a, the CH cases with  $W = 400$  Mm (same size symbols) and distance  $D = 150$  Mm (circle symbols) generate the dashed grey lines of null-point positions. The straight line with positive (negative) slope represents the cases with anti-aligned (aligned) polarity.

Also, for a given distance  $D$  (same symbol shape) and a given magnetic field strength  $B_0$  (same colour), a change in  $W$  (different sized circles) yields a curve that crosses the straight lines. For the aligned polarity cases, the larger the CH width, the higher the null-point position. Conversely, for the anti-aligned cases, the larger the CH width, the lower the height of the null point.

Moreover, for a given magnetic field strength  $B_0$  (same symbol colour) and a given parameter  $W$  (same symbol size) a change in the distance (different symbols) yields a curve that crosses the straight line. For the aligned polarity cases, the larger the distance, the lower the height of the null point. On the contrary, for the anti-aligned cases, the larger the distance, the higher the null-point location.

In Fig. 5b, a positive correlation can be seen between the magnetic force magnitude per unit length and the null-point distance ( $d$ ) to the FR. This correlation relies on the magnetic strength  $B_0$ , resulting in four different slopes (linking both polarities and FR configurations); the larger the magnetic field strength, the larger the slope. The anti-aligned cases are differentiated from the aligned ones by a black dot in the symbol centre.

This analysis sheds light on the relationships between null-point location, distance between CH and FR, the strength of the CH magnetic field, and CH area. A deeper study that considers a wider range of parameters would allow null-point locations to be predicted more precisely.

### 3. An observational case study

#### 3.1. Methods and techniques

To compare our model with observations, we analysed the trajectory of an eruptive prominence associated with a CME that occurred on April 30, 2012. During the outward motion of the prominence, the trajectory changed its direction twice; that is, the eruption suffered a double deflection. A nearby CH together with the eruptive prominence constitute a relatively isolated scenario that can be approximated by one of the schemes in Fig. 2. The eruption occurred to the east of the northern hemisphere starting at 04:06 UT. To reconstruct the 3D trajectory of the eruption, we track the prominence cold material by means of

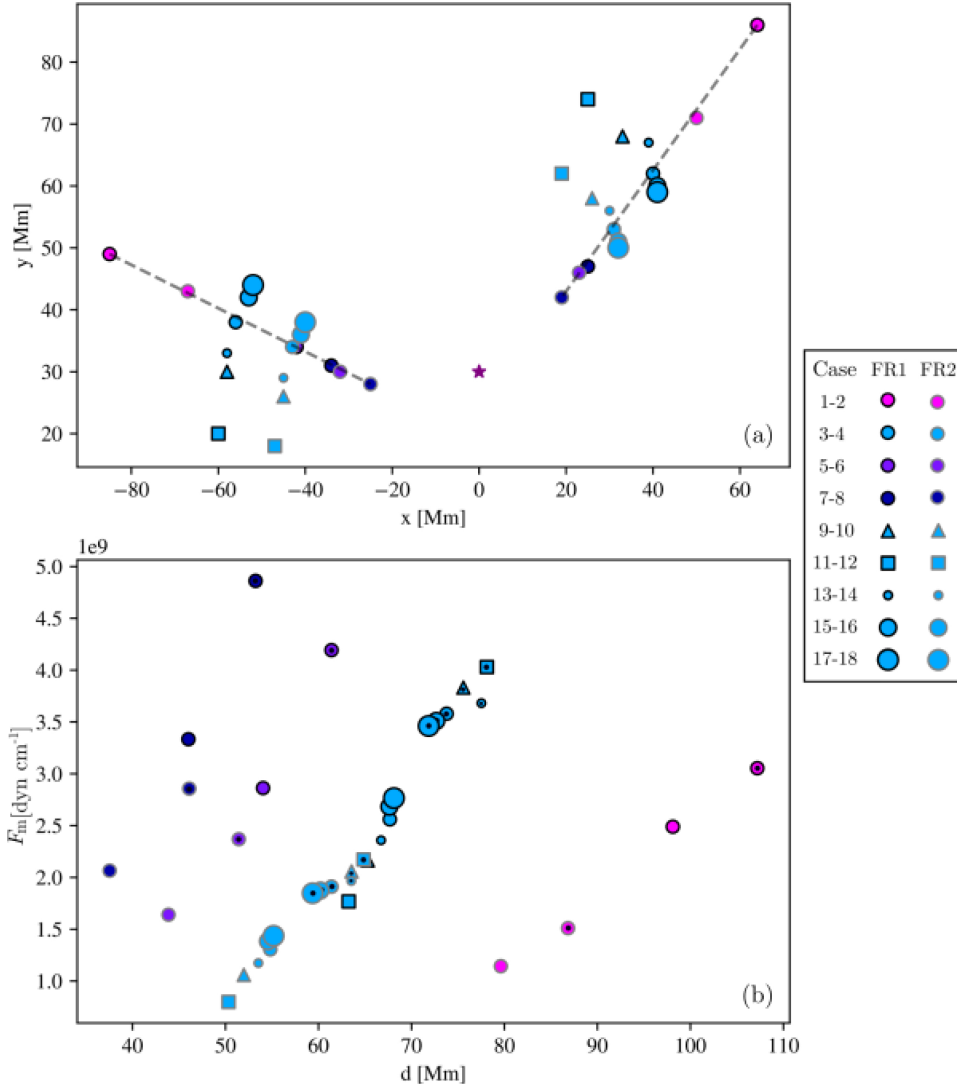


**Fig. 5.** (a) Null-point locations at  $t = 0$  s for all cases. The purple star represents the position of the FR, black edges correspond to FR1 simulations, and grey edges to FR2 ones. Dashed lines indicate the location of null points for aligned (left) and anti-aligned (right) cases, with the CH at the same distance  $D$  and same parameter  $W$ . The symbol colour changes with the strength  $B_0$  of the magnetic field (from weaker to stronger: pink, light blue, blue violet, and dark blue), the size changes with the parameter  $W$  (bigger means wider), and the shape changes with the distance  $D$  (from closer to farther: circle, triangle and square). (b) Module of the magnetic force per unit length versus null-point distance to the FR centre. Symbols have the same meanings as in (a). A black dot in the symbol centre indicates an anti-aligned case.

EUV images from the Extreme-Ultraviolet Imager (EUVI) of the SECCHI instrument suite (Sun-Earth Connection Coronal and Heliospheric Investigation, Howard et al. 2008) and white-light images from the SECCHI COR1 coronagraphs on board the STEREO A (ST-A) and STEREO B (ST-B) spacecraft. From 04:06 UT to 11:56 UT, we use EUVI 304 Å images from ST-A and ST-B. Running difference images from COR1 on board ST-A and ST-B are used to track the eruption at a later stage, from 11:45 UT to 13:30 UT.

We determined the global motion of the ejected prominence following its apex using the tie-pointing reconstruction technique (hereafter triangulation, Inhester 2006; Mierla et al. 2010). To allow for a better description of the trajectory, we consider a wide apex by triangulating three points from the prominence front at each analysed time (see plus symbols in the top panels of Fig. 6). The sequences of the three points follow the same trend, and therefore we consider that they accurately represent the global motion of the ejection. We tracked other points of the prominence and found that they also follow the same trend. In addition, we triangulate the prominence feet positions to estimate their location and length. The upper panels of Fig. 6 show the points representing the prominence feet (pink dot symbols) in addition to the points characterising the apex (white plus symbols) in the 304 Å filter of EUVI-A and EUVI-B; while the

lower panels of the figure show the prominence apex in COR1-A and COR1-B. To analyse the magnetic structure surrounding the ejection area, we use the Potential Field Source Surface (PFSS) model by Schrijver & De Rosa (2003).

### 3.2. Prominence evolution: trajectory and magnetic environment

The 3D trajectory determined by applying the triangulation method is displayed in Fig. 7. As can be seen from the figure, the eruption initially approaches the negative open magnetic field lines (blue lines, reconstructed from PFSS) and then moves away from it, following a new direction. The open magnetic field lines correspond to a CH that was catalogued as SPoCA 4548 (Barra et al. 2009; Verbeecq et al. 2014) when it was facing Earth on 4 April 2012. We measure the northeast and southwest feet of the erupting prominence on 30 April 2012 at  $t = 05:06$  UT and at a height  $R = 1.09 R_{\odot}$  and find them to be located at  $(67^{\circ}, 264^{\circ})$  and  $(60^{\circ}, 307^{\circ})$  respectively. The initial measured height, average latitude, and Carrington longitude of the prominence are  $(R_0, \theta_0, \phi_0) = (1.12 R_{\odot}, 61.6^{\circ}, 289.4^{\circ})$  at 04:06 UT (cyan point in Fig. 7 and cyan star in Fig. 8). The prominence apex then moves towards the closest minimum magnetic energy region, approaching the CH until  $(R_{cl}, \theta_{cl}, \phi_{cl}) = (1.45 R_{\odot}, 59.4^{\circ}, 278.1^{\circ})$

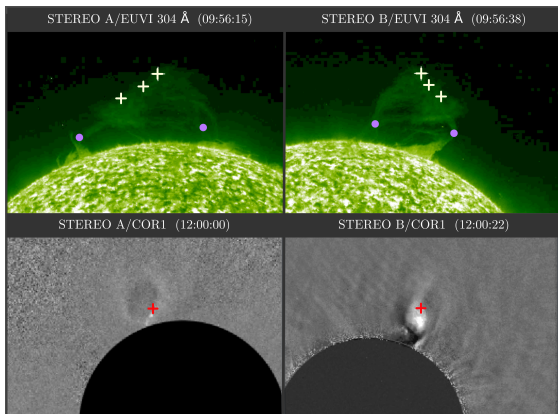


**Fig. 6.** Tie-pointing reconstruction of the 30 April 2012 prominence. The three white plus symbols in the *top panels* mark the wide apex considered in STEREO EUV images. The red plus symbol in the *bottom panels* show the apex in the STEREO coronagraph images.

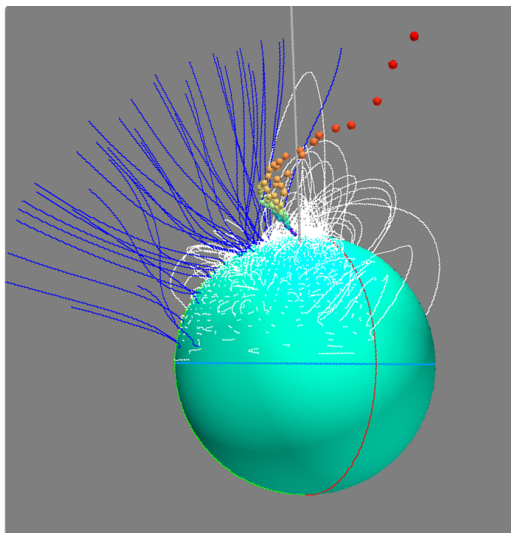


**Fig. 7.** Three-dimensional evolution of the prominence apex from 04:06 UT to 13:30 UT, from bluish to reddish spheres. The grey straight line represents the radial direction at the initial position of the apex. Blue lines belong to the open field lines of the CH and the white ones are the closed magnetic field lines. The red meridian points in direction of Earth, the green meridian in direction of STEREO B, and the light-blue line marks the solar equator.

at 10:46 UT (orange points in Fig. 7). Subsequently, the prominence apex deflects away from the CH towards the heliospheric current sheet and the final measured position is  $(R_f, \theta_f, \phi_f) = (2.67 R_\odot, 61.4^\circ, 336.8^\circ)$  at 13:30 UT (higher red point in Fig. 7 and red star in Fig. 8). Thus, the prominence suffers a double deflection: first it moves towards lower longitudes when approaching the CH (from  $289^\circ$  to  $278^\circ$ ) and afterwards it moves away from it, increasing its longitude from  $278^\circ$  to  $336^\circ$  and reaching the heliospheric current sheet.

The prominence erupts under the scenario described in Fig. 8. The figure shows a map of the magnetic field strength between  $200^\circ$  and  $340^\circ$ , where we indicate the magnetic structures as catalogued by the National Oceanic and Atmospheric Administration (NOAA) and Wilcox Solar Observatory (WSO) Source Surface Synoptic Charts. The pink shaded areas enclose the CHs, with size and location estimated from the open lines of the PFSS and the dark regions of the ST-B/EUVI 195 Å filter.

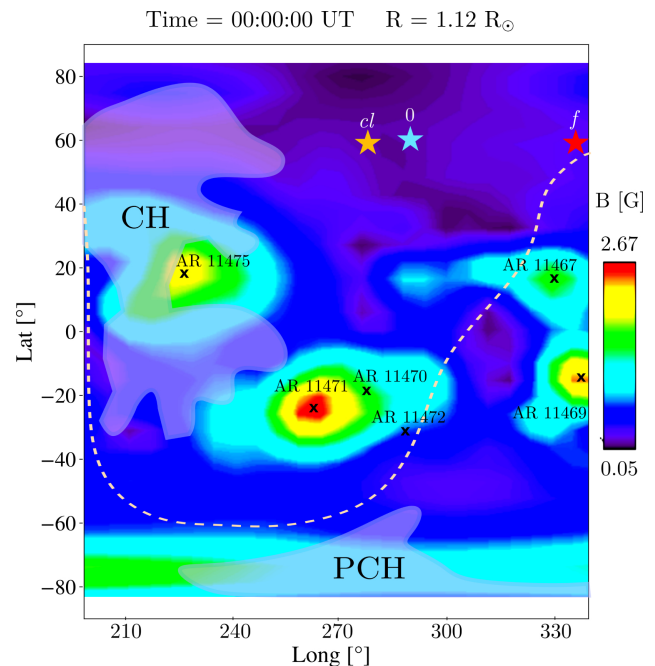


**Fig. 8.** Magnetic strength map at  $R = 1.12 R_\odot$  (initial height of the prominence), from longitude  $200^\circ$  to  $340^\circ$ , on 30 April 2012 at 00:00 UT. The stars represent the initial position (cyan), the closest position to the CH (orange), and the last measured (red) prominence position. The CHs, the active regions (NOAA), and the heliospheric current sheet (WSO) are superimposed on the map. PCH stands for polar coronal hole. The map has been provided by the Community Coordinated Modeling Center at Goddard Space Flight Center through their public Runs on Request system (<http://ccmc.gsfc.nasa.gov>) with the PFSS model.

The cyan star indicates the source region (SR), the orange star indicates the closest position to the CH, and the red star shows the last measured position. Several active regions can be seen in the map. We note that, as a result of the projection, AR 11467 may appear to be at a similar distance from the SR as the CH to the northeast, but in truth the nearest region of that AR (namely its eastern extension in cyan colour) is almost two times farther away than the nearest edge of the CH. The dashed line represents the heliospheric current sheet. Between the CH and the SR there is a zone of low magnetic strength (between the cyan and orange star). Figure 8 also shows a region of even lower magnetic strength towards the north and the southwest of the SR.

As the eruption took place at very high latitudes ( $\sim 60^\circ$ ) and close to the limb from Earth's perspective, the characterisation of the photospheric magnetic field was not straightforward. The identification of the polarities at both sides of the neutral line was based on the following reasoning, arising from Fig. 9. The figure depicts SDO/AIA coronal wavelengths overlapped to an SDO/HMI magnetogram, both at a time before eruption of the prominence. The prominence surrounded by a circular coronal cavity is seen above the north-northeast limb. At a later time, well after the eruption (starting ca. 12:00 UT), post eruptive loops can be discerned particularly in SDO/AIA 211 Å. These loops are not seen at the time of Fig. 9, but the approximate region where they form is encircled in the figure. More precisely, the loops form above the polarity inversion line seen as a dark channel ending at the prominence location, close to the limb. Therefore, it appears highly plausible that the eruptive prominence was sitting at that same neutral line, which enables identification of the magnetic field polarity at its sides. According to

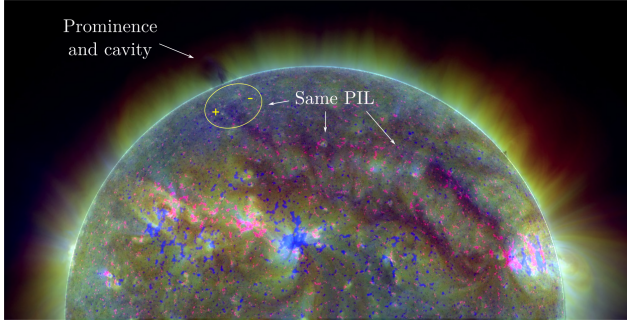


**Fig. 9.** SDO/AIA composite image of 211 Å, 193 Å, and 171 Å at 01:26 UT superimposed on a SDO/HMI image at 01:30 UT on the day of the event. In the latter, magenta and blue correspond to magnetic fields with positive and negative polarity, respectively. The prominence and its overlying cavity as well as the polarity inversion line (PIL) where the prominence presumably lies are indicated by arrows. The white circle denotes the region where post-eruptive loops form at a later time after eruption.

**Table 3.** Parameters used for the simulation of the observed event.

| Parameter                           | Values          |
|-------------------------------------|-----------------|
| $j_0$ (stA cm <sup>-2</sup> )       | 435             |
| $j_1$ (stA cm <sup>-2</sup> )       | 455             |
| $T_{\text{FR}}$ (MK)                | 0.8             |
| $n_c$ (cm <sup>-3</sup> )           | $3 \times 10^8$ |
| $n_{\text{CH}}$ (cm <sup>-3</sup> ) | $2 \times 10^8$ |
| $h_0$ (Mm)                          | 40              |
| $r$ (Mm)                            | 2.5             |
| $\Delta$ (Mm)                       | 0.25            |
| $d$ (Mm)                            | 3.125           |
| $M$                                 | 1               |
| $B_0$ (G)                           | -0.6            |
| $D$ (Mm)                            | 300             |
| $W$ (Mm)                            | 400             |

**Notes.** Parameters  $j_0$  and  $j_1$  are the current densities inside the FR in  $z$ -direction and in  $\phi$ -direction, respectively,  $T_{\text{FR}}$  is the internal FR temperature,  $n_c$  the numerical density at the base of the corona,  $n_{\text{CH}}$  the numerical density for the CH,  $h_0$  the vertical location (height) of the FR,  $r$  its radius, and  $\Delta$  the thickness of the transition layer between the FR interior and the corona. Parameters  $d$  and  $M$  are the depth of the line dipole below the boundary surface and its relative intensity, respectively. The CH parameters are  $B_0$ ,  $D$  and  $W$ .

the information provided by the SDO/HMI magnetogram, there is predominance of negative polarity to the northwest of the neutral line holding the prominence, and positive polarity to the southeast. This scenario, together with the fact that the magnetic field polarity of the CH is negative, suggests that this event is an example of an anti-aligned case.

### 3.3. Simulated event

From the observational event analysed in the previous section, the question arises as to whether or not it is possible that the mere presence of the CH results in the attraction of the FR structure. The numerical study carried out here together with information on the magnetic field configuration suggest that this may be the case if the FR and CH are magnetically anti-aligned.

Considering that the latitudinal displacement is negligible in comparison to the longitudinal one, we performed a simulation

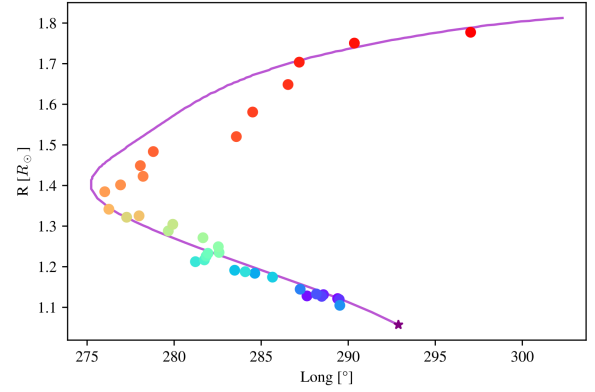


**Fig. 10.** Height versus average longitudinal deflection of the 30 April 2012 prominence (dots) and the trajectory of the simulated FR (solid line) with the purple star showing the initial FR centre position.

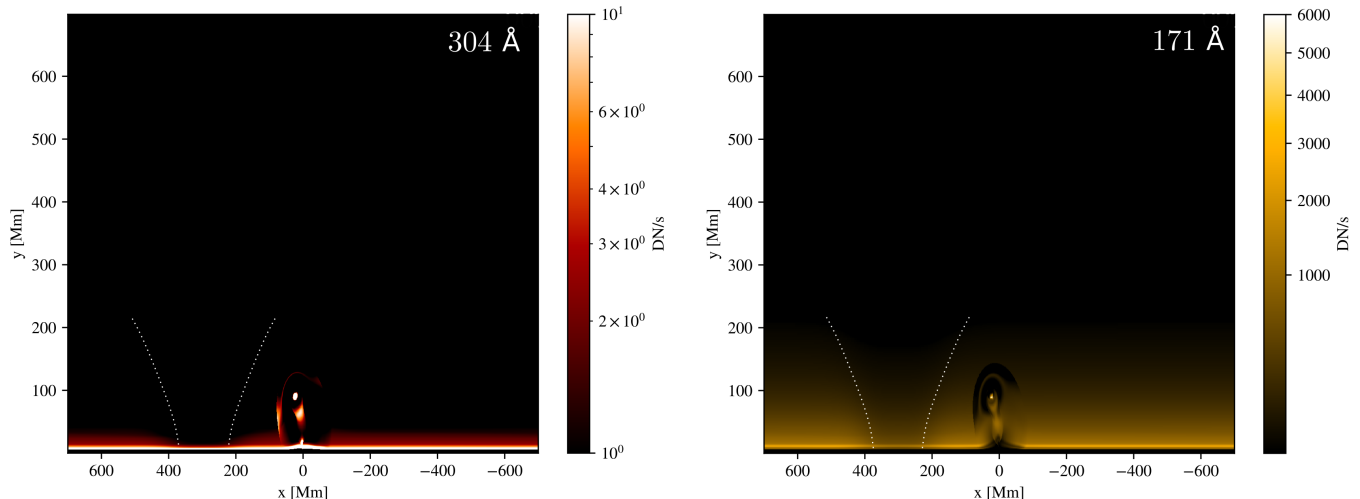
to emulate the deflection in the latter direction. The axis of the prominence is oriented along the northeast-southwest direction and its length is  $\sim 300$  Mm, which is large enough to assume a 2.5D approximation. Our model simulates the transverse motion projected on the longitudinal coordinate. Table 3 lists the parameters used for the simulation. We set the temperature  $T_{\text{FR}}$  to emulate the emission of the prominence in the corresponding EUV filters. The CH parameters are estimated from the magnetic maps ( $B_0$ ) and from the EUVI-B 195 Å filter ( $D$  and  $W$ ).

Figure 10 shows the average longitudinal deflection for the triangulated event (coloured dots), and the deflection of the simulated case (solid line). We note that a model of anti-aligned polarity is able to reproduce the deflection of the observed event. Taking into account that many effects are not considered in this simple model, the match between the simulation and the observation suggests that the proposed magnetic configuration is a possible cause of the prominence approach to the CH.

Figure 11 shows the synthetic emission in the 304 Å and 171 Å wavelengths generated by the FoMo tool (Van Doorselaere et al. 2016) at  $t = 200$  s. The code sets the thickness of simulation to 1 Mm because it is 2.5D. The subdense CH is set to the left of the FR structure, while the simulated FR is seen to emit in both wavelengths. The full evolution can be seen as an animation available [online](#). During its evolution, a subdense cavity is formed around the FR (clearly noticed in the 171 Å filter). The movie also shows the formation of waves and shocks.

## 4. Conclusions

Determining the mechanisms and the scenarios that produce deflections during the evolution of CMEs is a crucial step in improving space weather predictions. Many studies suggest that open magnetic fluxes behave as ‘magnetic walls’ that push CMEs away (e.g. Cremades et al. 2006; Gopalswamy et al. 2009; Gui et al. 2011; Céccere et al. 2020). However, there are a few reported events where the eruptions first approach open magnetic fluxes and then propagate away from them (Jiang et al. 2007; Yang et al. 2018; Sieyra et al. 2020). In these observational cases, the CME structure is not only close to a CH but also to other magnetic structures, such as an active region or a pseudostreamer, making it difficult to distinguish which of the structures are responsible for the double deflection and to what extent. Therefore, it is important to study cases in which the



**Fig. 11.** Synthetic EUV emission for filters 304 Å and 171 Å using the AIA response temperature. White dotted lines represent the estimated boundary of the CH. The animation of the full evolution is available [online](#).

FR–CH system is almost isolated, both observationally and numerically.

In our previous work (S20) we studied the FR–CH interaction numerically, simulating cases with aligned polarities between the two structures, and showing the importance of the null magnetic region in predicting the early evolution of the FR. Here, we used the same 2.5D model for which the FR–CH interaction could be studied in isolation. Through numerical simulations we find that the FRs evolve towards the null magnetic region whose position is determined by the FR and CH parameters. Particularly, the site where the null region is formed depends on the relative polarity alignment between FR and CH. During the early evolution of the system, the null point attracts the FR, in the aligned cases deflecting it away from the CH and in the anti-aligned cases causing the FR to approach the CH. However, as in many observational cases mentioned above, in their later evolution, all FRs move away from the CH, guided by the magnetic field, independently of the relative FR–CH polarity alignment. The physical mechanism is the same for both alignment cases, but the phenomenological result is different: in the low corona, the anti-aligned cases will exhibit a double-deflection trajectory, while the aligned cases will display a single deflection trajectory.

Performing several numerical simulations of different cases, varying FR properties and CH parameters, we find:

1. For a given CH width, at a given distance to the FR, there is a linear correlation between the position of the null point and the magnetic field strength. The larger the magnetic field strength, the closer the null point to the FR centre.
2. In the aligned (anti-aligned) cases, for a given distance and a given magnetic field strength, the larger the width, the higher (lower) the null-point location.
3. In the aligned (anti-aligned) cases, for a given magnetic field strength and a given width, the larger the distance, the lower (higher) the location of the null point.
4. There is a positive correlation between the magnetic force magnitude per unit length and the null-point distance to the FR. This correlation depends on the magnetic field strength: the larger the magnetic field strength, the larger the slope of the correlation.

To compare our model with observations, we analyse an event that occurred on 30 April 2012. We consider the system as

a relatively magnetically isolated scenario, where an ejected prominence is attracted by a nearby CH before it is deflected away from it. Careful analysis of AIA low coronal wavelengths together with HMI photospheric magnetic fields (see Fig. 9) reveals the magnetic polarities at the sides of the eruptive prominence. The analysis indicates that the magnetic polarities of the prominence source and of the CH are configured in an anti-aligned fashion. Assuming this particular alignment between both structures in a simple numerical model (where many effects were not considered) with approximate parameters estimated from the observations, we were able to reproduce the measured longitudinal deflection of the analysed event. This supports the conjecture that the presence of the CH and the magnetic topology that it produces are responsible for the double deflection of the event. We therefore propose that the null point first attracts the prominence towards the CH until the structure of the open magnetic fields deflects it away. Finally, the prominence follows the path of least resistance towards the heliospheric current sheet.

Although the scenarios in which the polarities are anti-aligned (see Sect. 2.3) seem to be common in the literature, most studies show that CMEs are deflected away from CHs. However, these facts are not necessarily incompatible. On one hand, most of the observational events analysed in the literature are restricted to the high coronal region, meaning that a CME could have approached a CH at an early stage, meaning that the double deflection would not necessarily have been reported. On the other hand, in studies that include the low corona, the deflection toward a CH may have been interpreted as the action of other magnetic structures pulling the CME towards the CH, without considering the mere presence of the CH as the possible cause of the attraction. Questions arise from the insights provided by the present study. For example, how common is the anti-aligned configuration? Is there a relation between the deflection rate and the FR–CH alignment? To answer these questions, more FR–CH interactions should be studied in detail at low coronal heights.

*Acknowledgements.* We thank the reviewer, Dr. Paulett Liewer, for her valuable suggestions that helped us to substantially improve the previous version of this manuscript. AS is doctoral fellow of CONICET. MC, AC and HC are members of the Carrera del Investigador Científico (CONICET). AS, MC and AC acknowledge support from ANPCyT under grant number PICT No. 2016-2480.

AS and MC also acknowledge support by SECYT-UNC grant number PC No. 33620180101147CB. HC acknowledges support from UTN grant UTI4915TC. Also, we thank the Centro de Cómputo de Alto Desempeño (UNC), where the simulations were carried out. Authors acknowledge use of data from STEREO (NASA) produced by the SECCHI consortium.

## References

- Barra, V., Delouille, V., Kretschmar, M., & Hochedez, J. F. 2009, *A&A*, **505**, 361
- Bemporad, A. 2009, *ApJ*, **701**, 298
- Berger, T. 2014, in *Nature of Prominences and their Role in Space Weather*, eds. B. Schmieder, J. M. Malherbe, & S. T. Wu, *IAU Symp.*, **300**, 15
- Cécere, M., Sieyra, M. V., Cremades, H., et al. 2020, *Adv. Space Res.*, **65**, 1654
- Cremades, H., Bothmer, V., & Tripathi, D. 2006, *Adv. Space Res.*, **38**, 461
- Filippov, B. P., Gopalswamy, N., & Lozhechkin, A. V. 2001, *Sol. Phys.*, **203**, 119
- Fryxell, B., Olson, K., Ricker, P., et al. 2000, *ApJS*, **131**, 273
- Gopalswamy, N., Mäkelä, P., Xie, H., Akiyama, S., & Yashiro, S. 2009, *J. Geophys. Res.: Space Phys.*, **114**, A00A22
- Gui, B., Shen, C., Wang, Y., et al. 2011, *Sol. Phys.*, **271**, 111
- Heinemann, S. G., Temmer, M., Heinemann, N., et al. 2019, *Sol. Phys.*, **294**, 144
- Hofmeister, S. J., Veronig, A., Reiss, M. A., et al. 2017, *ApJ*, **835**, 268
- Howard, R. A., Moses, J. D., Vourlidas, A., et al. 2008, *Space Sci. Rev.*, **136**, 67
- Inhester, B. 2006, ArXiv e-prints [arXiv:[astro-ph/0612649](https://arxiv.org/abs/astro-ph/0612649)]
- Jiang, Y., Yang, L., Li, K., & Shen, Y. 2007, *ApJ*, **667**, L105
- Kaiser, M. L., Kucera, T. A., Davila, J. M., et al. 2008, *Space Sci. Rev.*, **136**, 5
- Kay, C., Opher, M., & Evans, R. M. 2013, *ApJ*, **775**, 5
- Kay, C., Opher, M., & Evans, R. M. 2015, *ApJ*, **805**, 168
- Kay, C., Gopalswamy, N., Xie, H., & Yashiro, S. 2017, *Sol. Phys.*, **292**, 78
- Kilpua, E. K. J., Pomoell, J., Vourlidas, A., et al. 2009, *Ann. Geophys.*, **27**, 4491
- Krause, G., Cécere, M., Zurbriggen, E., et al. 2018, *MNRAS*, **474**, 770
- Liewer, P. C., Panasenco, O., & Hall, J. R. 2013, *Sol. Phys.*, **282**, 201
- Liewer, P., Panasenco, O., Vourlidas, A., & Colaninno, R. 2015, *Sol. Phys.*, **290**, 3343
- Lynch, B. J., & Edmondson, J. K. 2013, *ApJ*, **764**, 87
- Martin, S. F. 2003, *Adv. Space Res.*, **32**, 1883
- Mei, Z., Shen, C., Wu, N., et al. 2012, *MNRAS*, **425**, 2824
- Mierla, M., Inhester, B., Antunes, A., et al. 2010, *Ann. Geophys.*, **28**, 203
- Möstl, C., Rollett, T., Frahm, R. A., et al. 2015, *Nat. Commun.*, **6**, 7135
- Panasenco, O., & Martin, S. F. 2008, in *Subsurface and Atmospheric Influences on Solar Activity*, eds. R. Howe, R. W. Komm, K. S. Balasubramaniam, & G. J. D. Petrie, *ASP Conf. Ser.*, **383**, 243
- Panasenco, O., Martin, S., Joshi, A. D., & Srivastava, N. 2011, *J. Atmos. Solar-Terr. Phys.*, **73**, 1129
- Panasenco, O., Martin, S. F., Velli, M., & Vourlidas, A. 2013, *Sol. Phys.*, **287**, 391
- Pascoe, D. J., Nakariakov, V. M., & Kupriyanova, E. G. 2014, *A&A*, **568**, A20
- Pevtsov, A. A., Panasenco, O., & Martin, S. F. 2012, *Sol. Phys.*, **277**, 185
- Sahade, A., Cécere, M., & Krause, G. 2020, *ApJ*, **896**, 53
- Schrijver, C. J., & De Rosa, M. L. 2003, *Sol. Phys.*, **212**, 165
- Sieyra, M. V., Cécere, M., Cremades, H., et al. 2020, *Sol. Phys.*, **295**, 126
- Van Doorselaere, T., Antolin, P., Yuan, D., Reznikova, V., & Magyar, N. 2016, *Front. Astron. Space Sci.*, **3**, 4
- Verbeeck, C., Delouille, V., Mampaey, B., & De Visscher, R. 2014, *A&A*, **561**, A29
- Wang, R., Liu, Y. D., Dai, X., et al. 2015, *ApJ*, **814**, 80
- Xie, H., St. Cyr, O. C., Gopalswamy, N., et al. 2009, *Sol. Phys.*, **259**, 143
- Yang, J., Dai, J., Chen, H., Li, H., & Jiang, Y. 2018, *ApJ*, **862**, 86
- Zuccarello, F. P., Bemporad, A., Jacobs, C., et al. 2012, *ApJ*, **744**, 66